Geophysical Research Letters

RESEARCH LETTER
10.1029/2019GL084835

Key Points:
- We present shear wave velocities in the upper 300 m at the San Jacinto Fault, Clark segment
- The damage zone is asymmetric, with more damage to the northeast of the fault trace
- The damage zone geometry agrees with fault zone trapped waves generated by local earthquakes

Supporting Information:
- Supporting Information S1

Correspondence to:
Y. Wang,
yadong.wang@utah.edu

Citation:
Wang, Y., Allam, A., & Lin, F.-C. (2019). Imaging the Fault Damage Zone of the San Jacinto Fault Near Anza With Ambient Noise Tomography Using a Dense Nodal Array. *Geophysical Research Letters*, *46*. https://doi.org/10.1029/2019GL084835

Received 5 AUG 2019
Accepted 8 NOV 2019
Accepted article online 15 NOV 2019

Imaging the Fault Damage Zone of the San Jacinto Fault Near Anza With Ambient Noise Tomography Using a Dense Nodal Array

Yadong Wang[1], Amir Allam[1], and Fan-Chi Lin[1,2]

[1]Department of Geology and Geophysics, University of Utah, Salt Lake City, UT, USA, [2]Institute of Earth Sciences, Academia Sinica, Taipei, Taiwan

Abstract We apply the double-beamforming tomography to a monthlong temporary dense seismic array to obtain high-resolution images of the San Jacinto Fault's damage zone. We obtain Rayleigh waves between 0.3- and 0.8-s periods via vertical-vertical noise cross correlation, apply double beamforming to obtain phase velocities, and apply a piecewise 1-D least squares inversion to obtain shear velocities in the top 300 m. We observe a ~200-m-wide low-velocity zone that narrows with depth, which we interpret as the main damage zone in addition to two other ~100-m-wide subsidiary zones corresponding to secondary damaged structures, agreeing with the distribution of fault zone trapped waves produced by local earthquakes. The primary damage zone asymmetry indicates that materials on the northeast side of the fault are stiffer at seismogenic depth and suggests that large San Jacinto earthquakes tend to nucleate to the southeast and propagate to the northwest.

1. Introduction

1.1. Fault Zone Structure

Near-surface fault zone geometry is highly important for earthquake source locations, seismic hazard assessment, subsurface reservoir imaging, crustal hydrology, and so forth. The structure of damage zones—regions of highly fractured rocks surrounding faults—is particularly critical. Low-velocity fault damage zones can trap seismic energy and significantly amplify the ground motion (Ben-Zion & Aki, 1990; Qin et al., 2018; Qiu et al., 2017; Share et al., 2017). Coseismic wavefields can dynamically interact with damage zones to promote or inhibit earthquake ruptures (Weng et al., 2016). The dense fracture networks within damage zones can increase material permeability and influence fluid flow (Martel & Boger, 1998; Sibson, 1996; Wechsler et al., 2009). Damage zone width positively correlates with fault displacement (Faulkner et al., 2011; Mitchell & Faulkner, 2009; Savage & Brodsky, 2011), and damage zone asymmetry is strongly associated with preferred rupture propagation directions of large earthquakes (Ben-Zion & Shi, 2005; Dor et al., 2006; Perrin et al., 2016). Damage zone width decreases with depth (Allam et al., 2014; Sibson, 2003; Twiss & Moores, 2004) due to increasing normal stress, with the widest portion near the surface (Mitchell & Faulkner, 2009). Shear deformation within damage zones can accommodate a significant proportion of the slip during large earthquakes (Kaneko & Fialko, 2011; Milliner et al., 2015), which can lead to an underestimate of coseismic slip measured geodetically in damaged regions (Segall & Harris, 1986; Ryder & Burgmann, 2008). Thus, it is critical to properly characterize the shallow damage zone structure in order to accurately assess earthquake properties (Roten et al., 2017; Xu et al., 2015).

Passive body wave tomography can only resolve structures deeper than 2 km due to the distribution of seismic sources (e.g., Allam et al., 2014). Ambient noise tomography can potentially resolve near-surface features, but vertical and horizontal resolutions are often limited by interstation distance and the frequency content of coherent propagating signals (e.g., Lin et al., 2009). Resolving shallow structures with ambient noise requires dense seismometer networks and high-frequency surface waves that are usually more complicated due to scattering, multipathing, attenuation, and inhomogeneous noise sources. In this work, a recently developed double-beamforming tomography method (Wang et al., 2019) is applied, which can significantly enhance coherent signals and simultaneously retrieve velocity information. We measure Rayleigh wave phase from 1 to 3 Hz and invert for shear wave velocities in the upper 300 m with ~50-m resolution. This marks the first time this method has been used on a linear dense local array (Figure 1) to retrieve high-frequency surface waves and resolve local-scale structures at shallow depth.

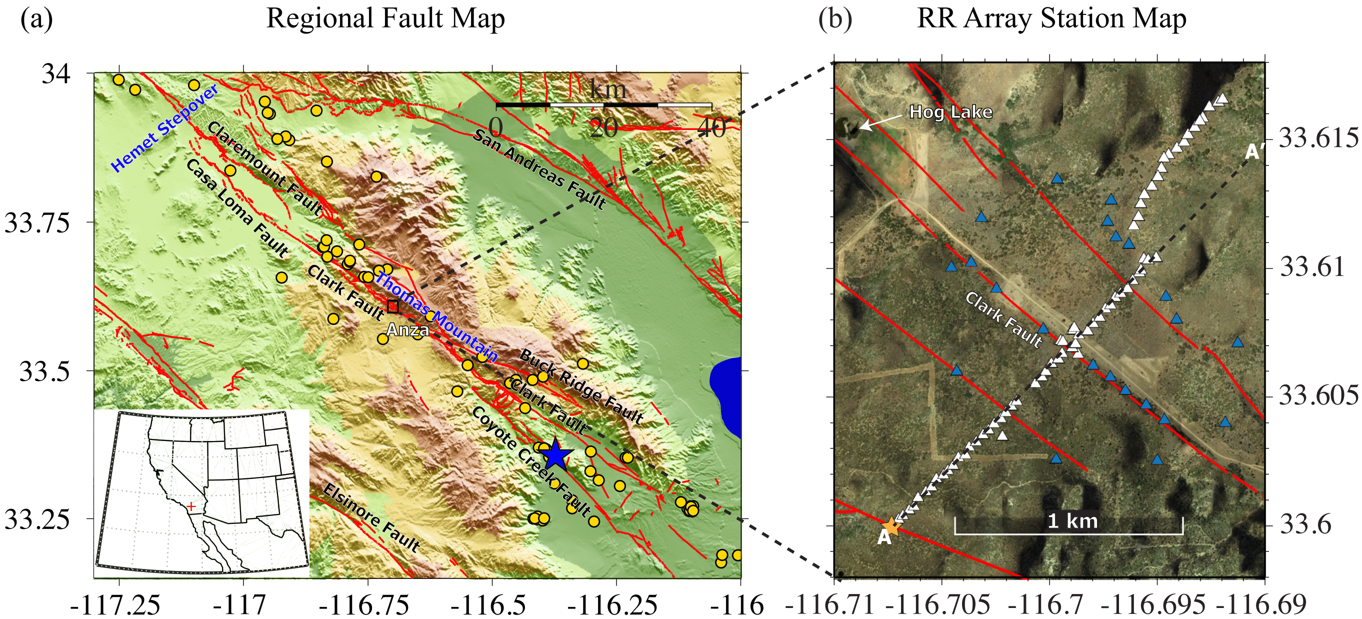

Figure 1. The San Jacinto Fault and station map. (a) The regional map of faults (red lines and black text; Treiman et al., 1999), geographic units (blue text), the 83 local earthquakes used in the trapped wave analysis (gold circles), and the M2.5 example earthquake shown in Figure 4a (blue star). (b) A zoomed view of the RR array, showing the stations used in this study (white triangles), unused stations (blue triangles), and the central station (orange star) of the record sections shown in Figure 2. The dashed line is the projected cross section shown in Figure 4, and the red lines show all mapped fault traces, though the Clark fault is the only major segment.

1.2. Geologic Setting

The San Jacinto fault is the most seismically active component of the Southern California plate boundary (Hauksson et al., 2012) and has produced at least 21 major earthquakes (Mw > 7) in the last 4,000 years according to paleoseismic studies at Hog Lake (Figure 1b; Rockwell et al., 2006; Rockwell et al., 2015). The significant hazard potential and complexity of the San Jacinto fault have motivated many geological and geomorphic observations (Dor, Rockwell, & Ben-Zion, 2006; Wechsler et al., 2009), regional-scale tomography with local body wave and ambient noise data (Allam et al., 2014; Allam & Ben-Zion, 2012; Fang et al., 2016; Zigone et al., 2015), bimaterial interface and damage zone imaging with small-aperture (up to ~2 km) linear nodal arrays (Lewis et al., 2005; Li & Vernon, 2001; Li et al., 2019; Qin et al., 2018; Qiu et al., 2017; Share et al., 2017; Share et al., 2019; Yang & Zhu, 2010; Yang et al., 2014; Zigone et al., 2019), and a rectangular single-component nodal array (Ben-Zion et al., 2015; Hillers et al., 2016; Roux et al., 2016; Qin et al., 2018; Mordret et al., 2019).

Our linear array of 71 three-component nodal seismometers (Figure 1a) is located 1 km from the Hog Lake paleoseismic site (Rockwell et al., 2015). The array straddles the Clark fault, one of the major slip-accommodating segments of the San Jacinto system and the only major active strand near Anza (Rockwell et al., 1990) (Fig 1b). The fault separates two geological units in the shallow crust: the high-velocity Cretaceous granite rocks of Thomas Mountain to the northeast and the low-velocity Pleistocene Bautista Formation and terrace deposits to the southwest (Rockwell et al., 2015; Sharp, 1967). Salisbury et al. (2012) estimated that this segment experiences the largest displacement during major earthquakes, with peak slip decreasing in both along-strike directions away from Hog Lake. Thus, the damage zone structure of this location is critical to understanding the behavior of large earthquakes on the San Jacinto fault. However, previous seismic imaging efforts have not fully characterized the damage zone structure due to either insufficient station spacing (Allam et al., 2014) or array aperture (Zigone et al., 2019).

In this work, we provide high-resolution shear wave velocity cross sections. In section 2, we describe the array configuration, data, and the procedures to measure Rayleigh wave phase velocities (section 2.2); invert for shear velocities (section 2.3); and calculate the energy of local earthquake trapped waves (section 2.4). Next, we present and discuss the phase and shear velocity results in section 3 and finally summarize the significance and implications of the results in section 4.

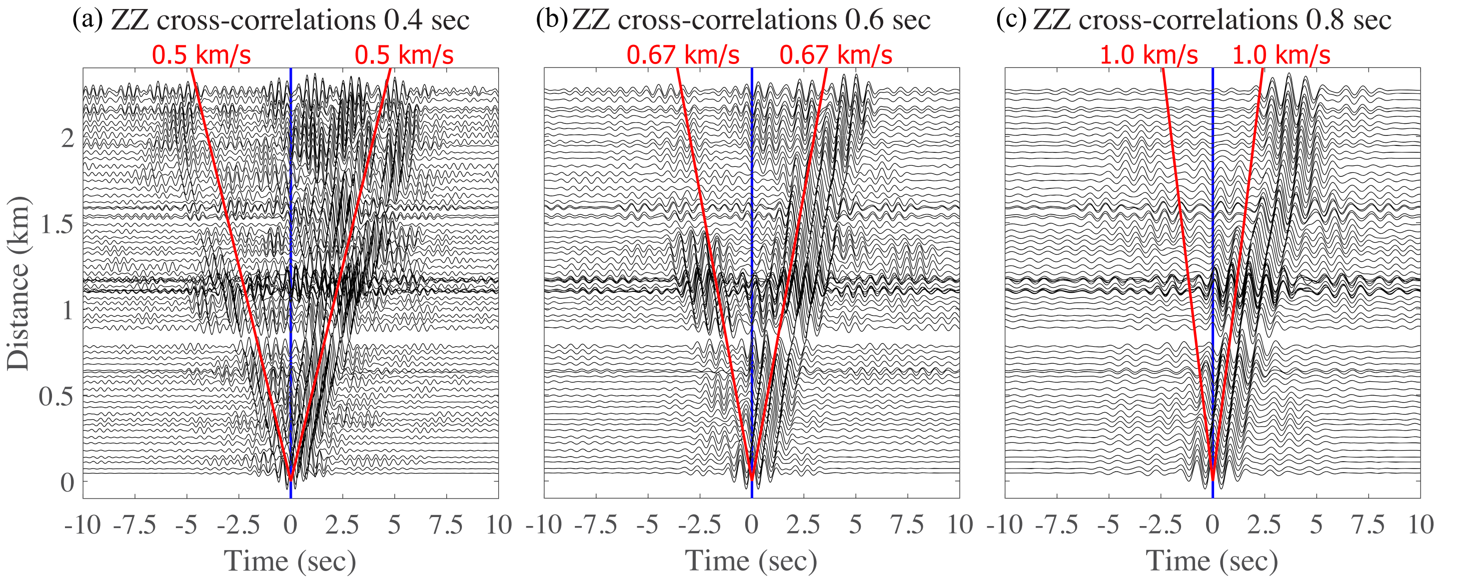

Figure 2. Vertical-vertical cross correlations from a source station (orange star in Figure 1b) to all receiver stations (white triangles in Figure 1b) at three period bands, with reference velocities shown in red.

2. Data and Methods

We deployed 94 three-component 5-Hz Fairfield geophones near Anza across the Clark segment of the San Jacinto fault (Figure 1b) from 16 September to 24 October 2016. The array had three parts: (1) an ~2.2-km line perpendicular to the fault trace, (2) an ~1-km line along the fault trace, and (3) a circular portion with ~0.5-km radius. In this study, we use ambient noise data and earthquake waveforms from 83 local events with magnitude >1.5 within 50-km distance. We only use the data of the 71 stations along the perpendicular line (Figure 1b), since we only aim to image high-resolution structures along this line in this study. Resolving structural variation along the fault using all stations but with lower resolution is beyond the scope of this study and will be the subject of future investigation. The portability, ease of use, and rugged durability of these seismic instruments made this work possible in single-day deployment and retrieval field trips.

2.1. Ambient Noise Cross Correlations

We follow Wang et al. (2019) to obtain monthlong stacked cross correlations from ambient noise data in 5-min windows. Clear fundamental Rayleigh waves are observed (Figure 2) on both positive and negative time lags at shorter periods (<0.6 s), but only on the positive time lag at longer periods (0.8 s), suggesting noise source distributions are period dependent. The stronger signals on the positive lags indicate the noise wavefield is likely dominated by the Pacific coastline. To further suppress the noise level, we stack the positive and negative time lags and construct the symmetric cross correlations used in the following analysis.

2.2. Double-Beamforming Tomography

We follow closely to the double-beamforming tomography method described by Wang et al. (2019) to measure Rayleigh wave phase velocities between 0.3- and 0.8-s periods across the array. Here, different from the previous study, the double beamforming process is performed in the frequency domain to avoid the precision limitation imposed by the sampling rate. In the time domain, uninterpolated waveforms can only be shifted by integer multiples of the sampling rate (in unit of seconds per point), but this limitation does not exist in the frequency domain. Because most of the stations used in this study follow line A-A′, we assume a single plane wave propagating between the source stations and the receiver stations to simplify the beamforming process. Tests with different assumed wavefronts (e.g., circular) showed no visible effect on the beamforming results.

For a source-beam center s_c and a receiver-beam center r_c, we select stations within 0.1 km of the source- and receiver-beam centers as sources s_i and receivers r_i, respectively. We require the interstation distance between every source-receiver pair to be longer than one wavelength of the Rayleigh waves to satisfy the far-field approximation (Wang et al., 2017; Yao et al., 2006). We use period-dependent velocity thresholds (0.5–1 km/s between 0.3- and 0.8-s periods; Figure 2) to cut and taper the cross correlations to suppress the body-wave/higher-mode contamination (Wang et al., 2019). Next, we normalize the cross correlations by their maximum amplitudes, transform them to the frequency domain, and stack them based on equation (1).

$$\mathrm{F}(u_s, u_r, \omega) = \frac{1}{N_s N_r} \sum_{i=1}^{N_s} \sum_{j=1}^{N_r} \mathrm{f}\left(s_i, r_j, \omega\right) \mathrm{e}^{-\mathrm{i}\omega\left(\tau_{s_i} + \tau_{r_j}\right)}, \tag{1}$$

where $\mathrm{f}(s_i, r_j, \omega)$ represents the cross-correlation function between stations s_i and r_j in the frequency domain, ω is angular frequency, N_s and N_r are the numbers of source and receiver stations, τ_{s_i} and τ_{r_j} are time shifts relative to the source and receiver beam centers defined by equations (2) and (3), u_s and u_r are the assumed Rayleigh wave phase slowness at the source and receiver sides, and $\mathrm{F}(u_s, u_r, \omega)$ is the beam-stacked cross correlation.

$$\tau_{s_i} = u_s(Xs_i - Xs_c)\sin\theta_s + u_s(Ys_i - Ys_c)\cos\theta_s, \tag{2}$$

$$\tau_{r_j} = u_r\left(Xr_j - Xr_c\right)\sin\theta_r + u_r\left(Yr_j - Yr_c\right)\cos\theta_r \tag{3}$$

Here, $(Xs_i - Xs_c)$ and $(Ys_i - Ys_c)$ represent the west-east and north-south distances between source station s_i and the source-beam center s_c, $(Xr_j - Xr_c)$ and $(Yr_j - Yr_c)$ represent the west-east and north-south distances between receiver station r_j and receiver-beam center r_c, and θ_s and θ_r are the propagating azimuths of the plane wave at the source beam center and the receiver beam center, respectively. In principle, the azimuthal terms can be solved along with the slowness parameters using 2-D distributed stations (e.g., Nakata et al., 2016). However, the 1-D configuration of the array used in this study limits us to assume a plane wave propagating along the great circle path to reduce the number of free parameters and avoid trade-off.

We next transform the beam-stacked cross-correlation $\mathrm{F}(u_s, u_r, \omega)$ back to the time domain and measure the beam power based on the maximum amplitude of the envelope function. A 2-D grid search of u_s and u_r is performed to find the highest beam powers at source and receiver beam centers. We require the signal-to-noise ratios (Lin et al., 2008) of the stacked waveforms to be higher than 12 to reject spurious measurements. At each beam center, we obtain repeated slowness measurements using multiple source/receiver beam combinations and calculate the mean slowness and the standard deviation of the mean (STDM) as the final slowness and its uncertainty, respectively. We compute the STDM as the standard deviation (STD) divided by the square root of the number of independent measurements (Wang et al., 2019). To obtain robust statistical results, we require the number of measurements to be larger than 10 at each location after removing outliers beyond two STD.

To account for the potential effect of topography, we fit the topography along the cross-section A-A′ within each beam with a straight line. Then we use the slope of the line to represent the average slope of the topography within that beam. Next, we correct the measured slowness and uncertainty using equations (4) and (5).

$$u_{corr} = u_{mean} \cdot \cos(\varphi) \tag{4}$$

$$e_{corr} = e \cdot \cos(\varphi) \tag{5}$$

Here φ is the angle of inclination of the line, u_{mean} and e are the mean slowness and its uncertainty, and u_{corr} and e_{corr} are the corrected slowness and uncertainty. We note that the differences between u_{mean} and u_{corr} are not significant as the angles of inclination are mostly smaller than 20°. The final phase velocity cross section and its associated uncertainties are summarized in Figure 3.

2.3. Shear Velocity Inversion

A piecewise 1-D uncertainty weighted iterative least squares inversion (Herrmann, 2013) with a constant velocity starting reference model is used to obtain shear velocities from the phase dispersions. We closely follow Wang et al. (2019) to perform the inversion at each location along the cross section. During the inversion process, we fix the Vp/Vs ratio as 1.75 and determine density based on the Vp value and the empirical relationship of Brocher (2005). To stabilize the inversion, we first impose a monotonicity constraint, which rejects models with reverse Vs with depth. We stop the inversion when changes in Vs models between

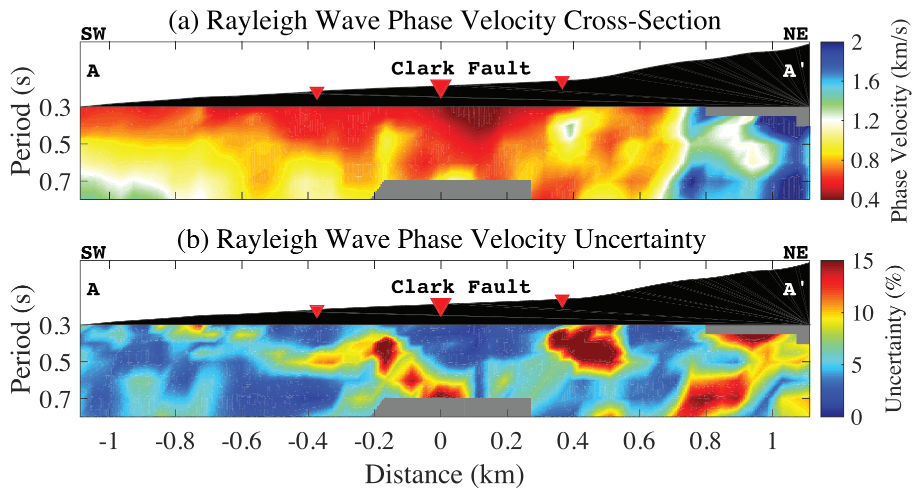

Figure 3. Rayleigh wave phase velocities and their associated uncertainties determined by double beamforming along the cross-section A-A′.

iterations are no longer visible. Then we perform a second round of inversion without the monotonicity constraint for locations where the reduced χ^2 misfit (Taylor, 1997) is greater than four. In the end, we combine piecewise 1-D Vs models (Figure S1 in the supporting information) from the first and second rounds of the inversion and accept models with reduced χ^2 misfit smaller than four to construct the 2-D Vs cross section (Figure 4c). Limited by the surface wave frequency range, we cut the Vs models at 300-m depth due to the lack of sensitivity at greater depth (Figure S2).

The model-predicted Rayleigh wave phase velocity cross section (Figure S3) is overall consistent with the measured phase velocity cross section (Figure 3a). Higher misfits are observed mostly at few locations and periods where uncertainties (Figure 3b) are relatively high (e.g., 0.5-s period at −0.2 km, 0.7-s period at 0 km, and 0.3- to 0.5-s periods at 0.4 km) and on the northeastern end of the profile (>0.8 km) where the array is no longer linear. The predicted phase velocity cross section is generally smoother than the observation, mainly due to the regularization (smoothing and damping) imposed in the inversion.

2.4. Trapped Wave Analysis

Coherent fault damage zones can produce trapped waves resulting from constructive interference of critically refracted seismic waves in a low-velocity layer (Ben-Zion, 1998; Ben-Zion & Aki, 1990). In this study, we analyze trapped waves from 83 local earthquakes occurred at different epicentral distances and with different magnitudes (Figure 1a) to validate the tomography results. Figure 4a shows the vertical-component 3-Hz low-passed waveforms from a M2.5 event (blue star in Figure 1a) as an example. We calculate the energy of the 3-Hz low-passed trapped waves as the integral of the squared envelope of the waveforms within 90 s of the event origin time. Although other phases are present in the earthquake wavefield (e.g., P and S), their contribution to the energy calculation is minimal. We then normalize the energy by the median energy across the array for each event and calculate the mean energy and the STD of the 83 events, after removing outliers beyond two STD. To eliminate significant contamination to trapped wave energy from human activity in this area (e.g., hiking and horse-riding), we remove stations with energy higher than 10 times the mean energy across the array for each event. Figure 4b presents the mean and the STD of the energy, as well as the energy of the example M2.5 event.

3. Results

3.1. Phase Velocities and Uncertainties

Figure 3 presents the variations in Rayleigh wave phase velocities and uncertainties with periods (0.3–0.8 s) and fault-normal distance. The most prominent low-velocity area is at 0 to 0.2 km between 0.3- and 0.5-s periods, while the highest velocities are near the northeast end of the array (>0.7 km). The phase velocities

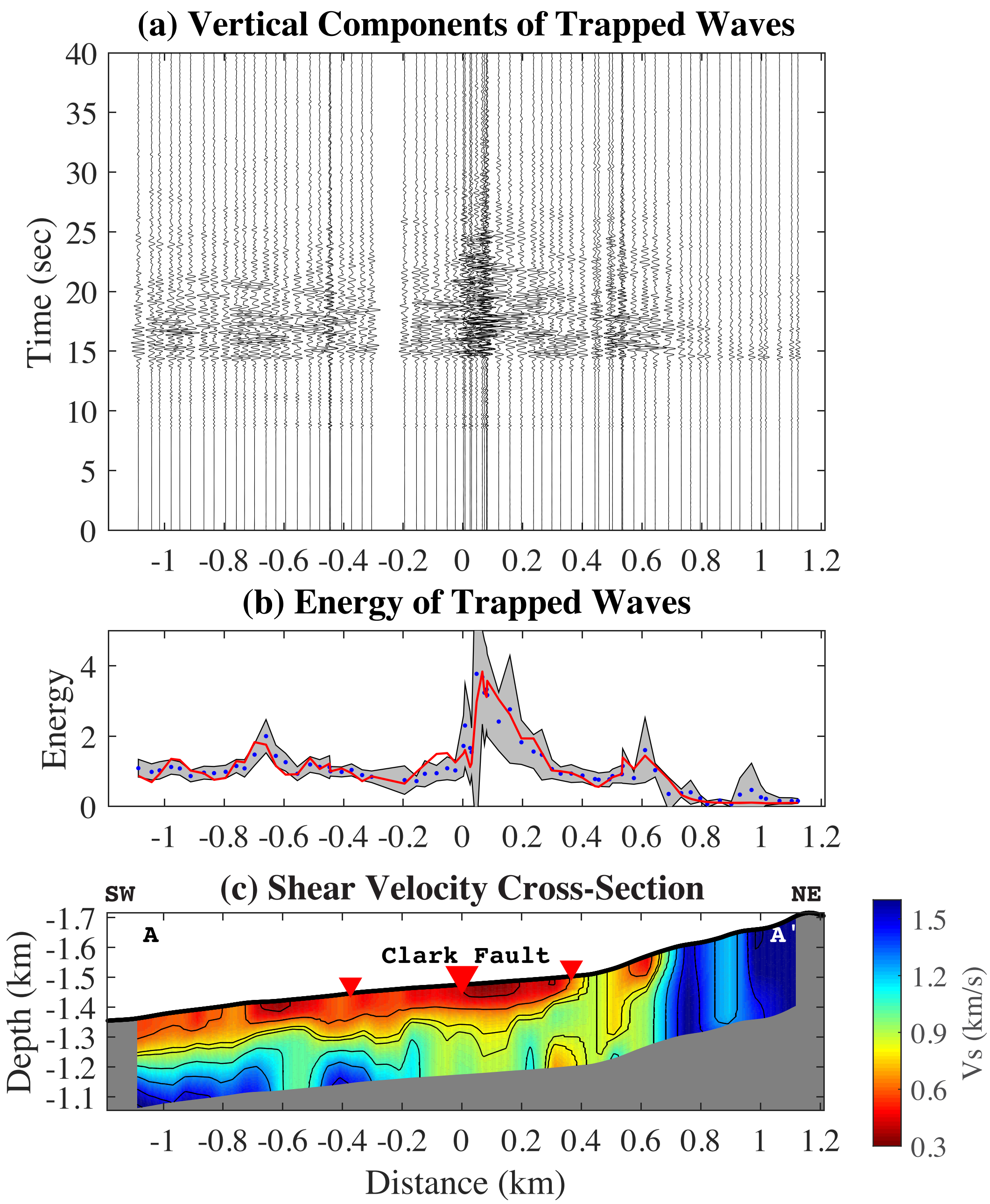

Figure 4. Shear wave velocities and trapped wave analysis. (a) The vertical component of the trapped waves from the example earthquake (Figure 1a) low-pass filtered at 3 Hz. (b) The energy of the trapped waves from the example M2.5 earthquake (red curve); averaged energy (blue dots) and STD (gray) of 83 local events. (c) The shear wave velocities along the cross-section A-A′.

generally increase with period except for a few anomalous regions (e.g., ~0.4 and ~0.8 km) where the uncertainties are relatively high. For example, very high uncertainties are observed at ~0.4-km distance between 0.3- and 0.5-s periods, due to abnormally low signal-to-noise ratios of the observed Rayleigh waves. Though it is unclear why the Rayleigh waves are weak in this zone, it could be related to the transition from low-velocity damage zone material to high-velocity intact material to the northeast (Figure 2) and/or affected by the interference of opposite-propagating waves (i.e., due to reflections). Since we weight the phase velocities by their uncertainties during the Vs inversion, the effects of these suspicious measurements on the final results are minimal.

3.2. Shear Wave Velocities

The final Vs cross section is presented in Figure 4c with fault-normal distance and depth. In general, velocities increase with distance from the fault trace, though the most prominent low-velocity zone is offset to the northeast of the Clark fault. There are two distinct smaller-scale low-velocity zones potentially associated with smaller-scale damaged structures. All of the low-velocity zones narrow with depth, featuring both minimum width and velocity reduction in the deepest portions imaged. In contrast to the low-velocity zones, the highest velocities are observed to the northeast within the intact Thomas Mountain Granite (Rockwell et al., 2015; Sharp, 1967), which has Vs > 1.5 km/s within the top 300 m.

3.3. Earthquake Trapped Waves

The waveforms for a single M2.5 event (Figure 4a) represent a clear example of fault zone trapped waves; the longest-duration and highest-amplitude arrivals are present in the central portion of the array and weaken with fault-normal distance in either direction. This pattern has been repeatedly observed both in real fault zones (e.g., Eccles et al., 2015; Ellsworth & Malin, 2011; Li & Vernon, 2001; Peng et al., 2003; Rovelli et al., 2002) and numerical simulations (e.g., Allam et al., 2015; Jahnke et al., 2002). The overall trapped wave energy pattern of 83 local events (Figure 4b) is extremely similar to that of a single event, with the highest energy present in the central portion of the array to the northeast of the surface trace of the Clark fault. In addition, there are two zones of elevated seismic energy (at −0.65 and 0.6 km), which spatially correspond to the subsidiary low-velocity zones that are presented in section 3.2.

4. Discussion

A complicated history of interaction between large seismic events and earth structure is recorded in the zone of damaged rock surrounding an active fault. Damage zones are the cumulative result of past earthquakes, which also control the properties of future events. Consequently, damage zone structures provide valuable insight into the earthquake behavior of a particular fault.

4.1. Damage Zone Width

Fault damage zone width scales with the cumulative displacement of the fault but usually only increases up to a few hundred meters (Faulkner et al., 2011), although exceptions exist (e.g., Cochran et al., 2009, claimed a 1.5-km-wide damage zone of the Calico fault in eastern California). The large range of variation in fault width can potentially be explained by the roughness properties of a given fault, which has been shown to affect normal stress both statically (e.g., Dieterich & Smith, 2009) and dynamically (Fang & Dunham, 2013). Therefore, a single fault even with homogeneous elastic properties can have significant along-fault variation in fault zone width simply due to changes in slip surface geometry (Johri et al., 2014). Specifically, regions of relatively simple fault geometry tend to have narrower damage zones, while regions with fault bends or step overs experience increased stresses resulting in more widespread damage (e.g., Finzi et al., 2009).

The present shear velocity results (Figure 4c) and fault zone trapped wave distribution (Figures 4a and 4b) are in strong agreement with respect to the width of the damage zone structure of the Clark fault near Anza. The ~200-m-wide primary damage zone is relatively narrow for a large-scale mature plate-bounding fault with >20-km cumulative slip (Kirby et al., 2007; Rockwell et al., 1990) given the expected scaling relationship (e.g., Mitchell et al., 2011). The relative narrowness of the damage zone here can be explained by the simplicity of the Anza segment of the Clark fault; large earthquakes tend to be confined to a single slip surface here (e.g., Rockwell et al., 2015) resulting in a relatively straight and geometrically simple segment (Sharp, 1967). This is in contrast to previous studies of the San Jacinto fault on the Hemet step over to the northeast (Li et al., 2019; Share et al., 2017; Share et al., 2019) and the Trifurcation to the southeast (Hillers et al., 2016; Qin et al., 2018; Mordret et al., 2019); both sites feature wider and more complicated damage zones and are located in regions with multiple major fault strands. Together with paleoseismological work showing that the Anza segment of the Clark fault experienced the largest coseismic slip during past M > 7.5 earthquakes (Rockwell et al., 2006; Rockwell et al., 2015; Salisbury et al., 2012) and numerical results examining the interaction of damage zone structures with earthquake ruptures (Dieterich & Smith, 2009; Fang & Dunham, 2013; Xu & Ben-Zion, 2017), our results support the interpretation that large earthquakes do not nucleate within the Anza segment and ruptures propagate smoothly at relatively high rupture velocity.

4.2. Damage Zone Asymmetry

Asymmetry of the damage zone with respect to surface trace has often been observed in large strike-slip and normal faults, which juxtapose materials of different seismic velocity (e.g., Berg & Skar, 2005; Dor et al., 2006; Mitchell et al., 2011). The asymmetry along these bimaterial interfaces can be explained by dynamic wave propagation effects: The P wavefront during earthquakes is advanced in the faster material, resulting in additional tension and thus more damage in the faster material (Ben-Zion & Shi, 2005; Duan, 2008; Ma, 2009). In addition to damage zone asymmetry, bimaterial interfaces also give rise to a preferred rupture direction: Rupture propagation is promoted in the direction of particle motion of the slower material (Ben-Zion & Shi, 2005). This bimaterial effect has been observed seismologically (e.g., Folesky et al., 2018; Kane et al., 2013; Kurzon et al., 2014; LenglinÈ & Got, 2011; Perrin et al., 2016) and geologically (Dor, Ben-Zion, et al., 2006; Mitchell et al., 2011; Wechsler et al., 2009).

Previous high-resolution tomographic images show that the Clark fault represents a strong bimaterial interface with the faster material on the northeastern side (Allam et al., 2014). Theoretical considerations predict a higher concentration of damage on the northeastern side of the fault (e.g., Xu & Ben-Zion, 2017); this is the exact pattern observed in the present imaging (Figure 4c) and trapped wave (Figure 4b) results. In addition, our results show that the undamaged rock 800 m to the northeast of the Clark fault trace has much higher seismic velocity than the material to the southwest, confirming the existence of a local bimaterial interface. This observed asymmetry in the present results is not likely affected by the uncertainty in the fault location; extensive paleoseismological work at the Hog Lake site about 1 km to the northwest accurately identified 21 large earthquakes with $M > 6.0$, allowing precise location of the principal slip surface (Rockwell et al., 2006; Rockwell et al., 2015). Thus, the present local-scale seismic imaging agrees with geological work (Rockwell et al., 2015), numerical simulations (Ben-Zion & Shi, 2005), seismic directivity analysis (Kurzon et al., 2014), and regional-scale tomographic work (Allam et al., 2014). Altogether, these results suggest that the largest earthquakes on the San Jacinto fault nucleate to the southeast—likely within the Trifurcation Area—and propagate to the northwest. Some evidence show that these ruptures may propagate through the Hemet step over and potentially onto the Southern San Andreas (Lozos, 2016; Lozos et al., 2015).

5. Conclusions

We have demonstrated that short-period (0.3–0.8 s) double-beamforming tomography from ambient noise can revealing complex shallow velocity structures (<300 m). The Vs profile reveals the damage structure of the Clark fault, including a ~200-m-wide asymmetric low-velocity zone. Compared to previous results at Blackburn Saddle (Li et al., 2019) to the northwest, we find the damage zone width increases to the northwest from Anza, reflecting the increase in fault geometrical complexity in this direction. Combined with previous geophysical, geological, and numerical results, our findings reinforce the idea that large San Jacinto earthquakes nucleate to the southeast and propagate to the northwest. This rupture direction results in amplified coseismic ground motion to the northwest due to the directivity effect, which leads to increased shaking in the highly populous Hemet, Riverside, and San Bernardino communities compared to a southeast propagating earthquake. Our results contribute to the understanding of earthquake properties and significant seismic hazard associated with the San Jacinto fault zone and encourage additional shallow seismic imaging studies of fault zones using dense seismometer arrays.

Acknowledgments

We thank Cooper Harris, Robert Zinke, Guanning Pang, Elizabeth Berg, Kevin Ward, Frank Vernon, Kathleen Ritterbush, Pieter-Ewald Share, and Hongrui Qiu for helping with the deployment of the RR array. The data are available through the International Federation of Digital Seismograph Networks (Allam, 2015). This study was supported by the National Science Foundation Grant EAR-1753362 and CyberSEES-1442665 and SCEC Awards 17229 and 19078.

References

Allam, A., Tape, C., & Ben-Zion, Y. (2015). Finite-frequency sensitivity kernels of seismic waves to fault zone structures. *Geophysical Journal International*, *203*, 2032–2048. https://doi.org/10.1093/gji/ggv413

Allam, A.A. (2015), San Jacinto damage zone imaging arrays. International Federation of Digital Seismograph Networks. Dataset/Seismic Network. Doi: https://doi.org/10.7914/SN/9K_2015

Allam, A. A., & Ben-Zion, Y. (2012). Seismic velocity structures in the southern California plate-boundary environment from double-difference tomography. *Geophysical Journal International*, *190*, 1181–1196. https://doi.org/10.1111/j.1365-246X.2012.05544.x

Allam, A. A., Ben-Zion, Y., Kurzon, I., & Vernon, F. (2014). Seismic velocity structure in the Hot Springs and Trifurcation areas of the San Jacinto fault zone, California, from double-difference tomography. *Geophysical Journal International*, *198*, 978–999. https://doi.org/10.1093/gji/ggu176

Ben-Zion, Y. (1998). Properties of seismic fault zone waves and their utility for imaging low-velocity structures. *Journal of Geophysical Research*, *103*, 12,567–12,585. https://doi.org/10.1029/98jb00768

Ben-Zion, Y., & Aki, K. (1990). Seismic radiation from an *SH* line source in a laterally heterogeneous planar fault. *Bulletin of the Seismological Society of America*, *80*, 971–994.

Ben-Zion, Y., & Shi, Z. (2005). Dynamic rupture on a material interface with spontaneous generation of plastic strain in the bulk. *Earth and Planetary Science Letters*, *236*, 486–496. https://doi.org/10.1016/j.epsl.2005.03.025

Ben-Zion, Y., Vernon, F. L., Ozakin, Y., Zigone, D., Ross, Z. E., Meng, H., et al. (2015). Basic data features and results from a spatially dense seismic array on the San Jacinto fault zone. *Geophysical Journal International*, *202*(1), 370–380. https://doi.org/10.1093/gji/ggv142

Berg, S., & Skar, T. (2005). Controls on damage zone asymmetry of a normal fault zone: Outcrop analyses of a segment of the Moab fault, SE Utah. *Journal of Structural Geology*, *27*, 1803–1822. https://doi.org/10.1016/j.jsg.2005.04.012

Brocher, T. M. (2005). Empirical relations between elastic wavespeeds and density in the Earth's crust. *Bulletin of the Seismological Society of America*, *95*(6), 2081–2092. https://doi.org/10.1785/0120050077

Cochran, E. S., Li, Y.-G., Shearer, P. M., Barbot, S., Fialko, Y., & Vidale, J. E. (2009). Seismic and geodetic evidence for extensive, long-lived fault damage zones. *Geology*, *37*, 315–318. https://doi.org/10.1130/G25306A.1

Dieterich, J. H., & Smith, D. E. (2009). Nonplanar faults: Mechanics of slip and off-fault damage. *Pure and Applied Geophysics*, *166*(10-11), 1799–1815. https://doi.org/10.1007/s00024-009-0517-y

Dor, O., Ben-Zion, Y., Rockwell, T. K., & Brune, J. (2006). Pulverized rocks in the Mojave section of the San Andreas Fault Zone. *Earth and Planetary Science Letters*, *245*, 642–654. https://doi.org/10.1016/j.epsl.2006.03.034

Dor, O., Rockwell, T. K., & Ben-Zion, Y. (2006). Geological observations of damage asymmetry in the structure of the San Jacinto, San Andreas and Punchbowl faults in Southern California: A possible indicator for preferred rupture propagation direction. *Pure and Applied Geophysics*, *163*, 301–349. https://doi.org/10.1007/s00024-005-0023-9

Duan, B. (2008). Asymmetric off-fault damage generated by bilateral ruptures along a bimaterial interface. *Geophysical Research Letters*, *35*, L14306. https://doi.org/10.1029/2008GL034797

Eccles, J. D., Gulley, A. K., Malin, P. E., Boese, C. M., Townend, J., & Sutherland, R. (2015). Fault zone guided wave generation on the locked, late interseismic Alpine fault, New Zealand. *Geophysical Research Letters*, *42*, 5736–5743. https://doi.org/10.1002/2015GL064208

Ellsworth, W. L., & Malin, P. E. (2011). Deep rock damage in the San Andreas Fault revealed by P-and S-type fault-zone-guided waves. *Geological Society, London, Special Publications*, *359*(1), 39–53.

Fang, H., Zhang, H., Yao, H., Allam, A., Zigone, D., Ben-Zion, Y., et al. (2016). A new algorithm for three-dimensional joint inversion of body wave and surface wave data and its application to the Southern California plate boundary region. *Journal of Geophysical Research: Solid Earth*, *121*, 3557–3569. https://doi.org/10.1002/2015JB012702

Fang, Z., & Dunham, E. M. (2013). Additional shear resistance from fault roughness and stress levels on geometrically complex faults. *Journal of Geophysical Research: Solid Earth*, *118*, 3642–3654. https://doi.org/10.1002/jgrb.50262

Faulkner, D. R., Mitchell, T. M., Jensen, E., & Cembrano, J. (2011). Scaling of fault damage zones with displacement and the implications for fault growth processes. *Journal of Geophysical Research*, *116*, B05403. https://doi.org/10.1029/2010JB007788

Finzi, Y., Hearn, E. H., Ben-Zion, Y., & Lyakhovsky, V. (2009). Structural properties and deformation patterns of evolving strike-slip faults: Numerical simulations incorporating damage rheology. *Pure and Applied Geophysics*, *166*, 1537–1573. https://doi.org/10.1007/s00024-009-0522-1

Folesky, J., Kummerow, J., & Shapiro, S. A. (2018). Patterns of Rupture Directivity of Subduction Zone Earthquakes in Northern Chile. *Journal of Geophysical Research: Solid Earth*, *123*, 10–785. https://doi.org/10.1029/2018JB016331

Hauksson, E., Yang, W., & Shearer, P. M. (2012). Waveform Relocated Earthquake Catalog for Southern California (1981 to 2011). *Bulletin of the Seismological Society of America*, *102*(5), 2239–2244.

Herrmann, R. B. (2013). Computer programs in seismology: An evolving tool for instruction and research. *Seismological Research Letters*, *84*, 1081–1088. https://doi.org/10.1785/0220110096

Hillers, G., Roux, P., Campillo, M., & Ben-Zion, Y. (2016). Focal spot imaging based on zero lag cross-correlation amplitude fields: Application to dense array data at the San Jacinto fault zone. *Journal of Geophysical Research: Solid Earth*, *121*, 8048–8067. https://doi.org/10.1002/2016JB013014

Jahnke, G., Igel, H., & Ben-Zion, Y. (2002). Three-dimensional calculations of fault-zone-guided waves in various irregular structures. *Geophysical Journal International*, *151*(2), 416–426. https://doi.org/10.1046/j.1365-246X.2002.01784.x

Johri, M., Dunham, E. M., Zoback, M. D., & Fang, Z. (2014). Predicting fault damage zones by modeling dynamic rupture propagation and comparison with field observations. *Journal of Geophysical Research: Solid Earth*, *119*, 1251–1272. https://doi.org/10.1002/2013JB010335

Kane, D. L., Shearer, P. M., Goertz-Allmann, B. P., & Vernon, F. L. (2013). Rupture directivity of small earthquakes at Parkfield. *Journal of Geophysical Research: Solid Earth*, *118*, 212–221. https://doi.org/10.1029/2012JB009675

Kaneko, Y., & Fialko, Y. (2011). Shallow slip deficit due to large strike-slip earthquakes in dynamic rupture simulations with elasto-plastic off-fault response. *Geophysical Journal International*, *186*(3), 1389–1403.

Kirby, S. M., Janecke, S. U., Dorsey, R. J., Housen, B. A., McDougall, K., Langenheim, V., & Steely, A. (2007). Pleistocene Brawley and Ocotillo formations: evidence for initial strike-slip deformation along the San Felipe and San Jacinto fault zones, California. *Journal of Geology*, *115*, 43–62. https://doi.org/10.1086/509248

Kurzon, I., Vernon, F. L., Ben-Zion, Y., & Atkinson, G. (2014). Ground motion prediction equations in the San Jacinto fault zone: Significant effects of rupture directivity and fault zone amplification. *Pure and Applied Geophysics*, *171*(11), 3045–3081.

LenglinÈ, O., & Got, J.-L. (2011). Rupture directivity of microearthquake sequences near Parkfield, California. *Geophysical Research Letters*, *38*, L08310. https://doi.org/10.1029/2011GL047303

Lewis, M. A., Peng, Z., Ben-Zion, Y., & Vernon, F. L. (2005). Shallow seismic trapping structure in the San Jacinto fault zone near Anza, California. *Geophysical Journal International*, *162*, 867–881. https://doi.org/10.1111/j.1365-246X.2005.02684.x

Li, J., Lin, F.-C., Allam, A., Ben-Zion, Y., Liu, Z., & Schuster, G. (2019). Wave equation dispersion inversion of surface waves recorded on irregular topography. *Geophysical Journal International*, *217*(1), 346–360. https://doi.org/10.1093/gji/ggz005

Li, Y.-G., & Vernon, F. L. (2001). Characterization of the San Jacinto fault zone near Anza, California, by fault zone trapped waves. *Journal of Geophysical Research*, *106*, 30671–30688. https://doi.org/10.1029/2000JB000107

Lin, F. C., Moschetti, M. P., & Ritzwoller, M. H. (2008). Surface wave tomography of the western United States from ambient seismic noise: Rayleigh and Love wave phase velocity maps. *Geophysical Journal International*, *173*, 281–298. https://doi.org/10.1111/j.1365-246X.2008.03720.x

Lin, F. C., Ritzwoller, M. H., & Snieder, R. (2009). Eikonal tomography: Surface wave tomography by phase front tracking across a regional broad-band seismic array. *Geophysical Journal International*, *177*(3), 1091–1110. https://doi.org/10.1111/j.1365-246X.2009.04105.x

Lozos, J. C. (2016). A case for historic joint rupture of the San Andreas and San Jacinto faults. *Science Advances*, *2*(3).
Lozos, J. C., Oglesby, D. D., Brune, J. N., & Olsen, K. B. (2015). Rupture and ground-motion models on the northern San Jacinto fault, incorporating realistic complexity. *Bulletin of the Seismological Society of America*, *105*(4), 1931–1946.
Ma, S. (2009). Distinct asymmetry in rupture-induced inelastic strain across dipping faults: An off-fault yielding model. *Geophysical Research Letters*, *36*, L20317. https://doi.org/10.1029/2009GL040666
Martel, S. J., & Boger, W. A. (1998). Geometry and mechanics of secondary fracturing around small three-dimensional faults in granitic rock. *Journal of Geophysical Research*, *103*, 21,299–21,314.
Milliner, C. W., Dolan, J. F., Hollingsworth, J., Leprince, S., Ayoub, F., & Sammis, C. G. (2015). Quantifying near-field and off-fault deformation patterns of the 1992 Mw 7.3 landers earthquake. *Geochemistry, Geophysics, Geosystems*, *16*, 1577–1598. https://doi.org/10.1002/2014GC005693
Mitchell, T. M., Ben-Zion, Y., & Shimamoto, T. (2011). Pulverized fault rocks and damage asymmetry along the Arima-Takatsuki Tectonic Line, Japan. *Earth and Planetary Science Letters*, *308*, 284–297. https://doi.org/10.1016/j.epsl.2011.04.023
Mitchell, T. M., & Faulkner, D. R. (2009). The nature and origin of off fault damage surrounding strike-slip fault zones with a wide range of displacements: A field study from the Atacama fault zone, northern Chile. *Journal of Structural Geology*, *31*(8), 802–816. https://doi.org/10.1016/j.jsg.2009.05.002
Mordret, A., Roux, P., Boué, P., & Ben-Zion, Y. (2019). Shallow three-dimensional structure of the San Jacinto fault zone revealed from ambient noise imaging with a dense seismic array. *Geophysical Journal International*, *216*, 896–905. https://doi.org/10.1093/gji/ggy464
Nakata, N., Boue, P., Brenguier, F., Roux, P., Ferrazzini, V., & Campillo, M. (2016). Body and surface wave reconstruction from seismic noise correlations between arrays at Piton de la Fournaise volcano. *Geophysical Research Letters*, *43*, 1047–1054. https://doi.org/10.1002/2015GL066997
Peng, Z., Ben-Zion, Y., Michael, A. J., & Zhu, L. (2003). Quantitative analysis of seismic fault zone waves in the rupture zone of the 1992 Landers, California, earthquake: evidence for a shallow trapping structure. *Geophysical Journal International*, *155*(3), 1021–1041.
Perrin, C., Manighetti, I., Ampuero, J.-P., Cappa, F., & Gaudemer, Y. (2016). Location of largest earthquake slip and fast rupture controlled by along-strike change in fault structural maturity due to fault growth. *Geophys. Res Solid Earth*, *121*, 3666–3685. https://doi.org/10.1002/2015JB012671
Qin, L., Ben-Zion, Y., Qiu, H., Share, P. E., Ross, Z. E., & Vernon, F. L. (2018). Internal structure of the San Jacinto fault zone in the trifurcation area southeast of Anza, California, from data of dense seismic arrays. *Geophysical Journal International*, *213*, 98–114. https://doi.org/10.1093/gji/ggx540
Qiu, H., Ben-Zion, Y., Ross, Z. E., Share, P.-E., & Vernon, F. L. (2017). Internal structure of the San Jacinto fault zone at Jackass Flat from data recorded by a dense linear array. *Geophysical Journal International*, *209*, 1369–1388. https://doi.org/10.1093/gji/ggx096
Rockwell, T. K., Dawson, T. E., Young Ben-Horin, J., & Seitz, G. (2015). A 21-event, 4,000-year history of surface ruptures in the Anza seismic gap, San Jacinto fault, and implications for long-term earthquake production on a major plate boundary fault. *Pure and Applied Geophysics*, *172*(5), 1143–1165. https://doi.org/10.1007/s00024-014-0955-z
Rockwell, T., Loughman, C., & Merifield, P. (1990). Late Quaternary rate of slip along the San Jacinto Fault Zone near Anza, southern California. *Journal of Geophysical Research*, *95*, 8593–8605. https://doi.org/10.1029/JB095iB06p08593
Rockwell, T. K., Seitz, G., Dawson, T., & Young, J. (2006). The long record of San Jacinto fault paleoearthquakes at Hog Lake: Implications for regional patterns of strain release in the southern San Andreas fault system. *Seismological Research Letters*, *77*(2), 270.
Roten, D., Olsen, K., Cui, Y., & Day, S. (2017). Quantification of fault zone plasticity effects with spontaneous rupture simulations. *Pure and Applied Geophysics*, 1–23. https://doi.org/10.1007/s00024-017-1466-5
Roux, P., Moreau, L., Lecointre, A., Hillers, G., Campillo, M., Ben-Zion, Y., et al. (2016). A methodological approach towards high-resolution surface wave imaging of the san jacinto fault zone using ambient-noise recordings at a spatially dense array. *Geophysical Journal International*, *206*(2), 980–992. https://doi.org/10.1093/gji/ggw193
Rovelli, A., Caserta, A., Marra, F., & Ruggiero, V. (2002). Can seismic waves be trapped inside an inactive fault zone? The case study of Nocera Umbra, central Italy. *Bulletin of the Seismological Society of America*, *92*(6), 2217–2232.
Ryder, I., & Burgmann, R. (2008). Spatial variations in slip deficit on the central San Andreas Fault from InSAR. *Geophysical Journal International*, *175*, 837–852. https://doi.org/10.1111/j.1365-246X.2008.03938.x
Salisbury, J. B., Rockwell, T. K., Middleton, T. J., & Hudnut, K. W. (2012). LiDAR and field observations of slip distribution for the most recent surface ruptures along the central San Jacinto fault. *Bulletin of the Seismological Society of America*, *102*, 598–619.
Savage, H. M., & Brodsky, E. E. (2011). Collateral damage: Evolution with displacement of fracture distribution and secondary fault strands in fault damage zones. *Journal of Geophysical Research*, *116*, B03405. https://doi.org/10.1029/2010JB007665
Segall, P., & Harris, R. (1986). Slip Deficit on the San Andreas Fault at Parkfield, California, as Revealed by Inversion of Geodetic Data. *Science*, *233*(4771), 1409–1413. https://doi.org/10.1126/science.233.4771.1409
Share, P.-E., Allam, A. A., Ben-Zion, Y., Lin, F.-C., & Vernon, F. L. (2019). Structural properties of the San Jacinto fault zone at Blackburn Saddle from seismic data of a dense linear array. *Pure and Applied Geophysics*, *176*(3), 1169–1191. https://doi.org/10.1007/s00024-018-1988-5
Share, P. E., Ben-Zion, Y., Ross, Z. E., Qiu, H., & Vernon, F. L. (2017). Internal structure of the San Jacinto fault zone at Blackburn Saddle from seismic data of a linear array. *Geophysical Journal International*, *210*, 819–832. https://doi.org/10.1093/gji/ggx191
Sharp, R. V. (1967). San Jacinto fault zone in the peninsular ranges of Southern California. *GSA Bulletin*, *78*, 705–730. https://doi.org/10.1130/0016-7606(1967)78[705:SJFZIT]2.0.CO;2
Sibson, R. H. (1996). Structural permeability of fluid-driven fault-fracture meshes. *Journal of Structural Geology*, *18*, 1031–1042.
Sibson, R. H. (2003). Thickness of the seismic slip zone. *Bulletin of the Seismological Society of America*, *93*(3), 1169–1178. https://doi.org/10.1785/0120020061
Taylor, J. R. (1997). *An introduction to error analysis: The study of the uncertainties in physical measurements* (p. 271). Sausalito, CA: University Science.
Treiman, J.A., & Lundberg, M., compilers (1999). Fault number 125c, San Jacinto fault, Anza section, in Quaternary fault and fold database of the United States: U.S. Geological Survey website
Twiss, R., & Moores, E. (2004). *Structural Geology*, 2nd ed., W.H. Freemanand Co.
Wang, Y., Lin, F.-C., Schmandt, B., & Farrell, J. (2017). Ambient noise tomography across Mount St. Helens using a dense seismic array. *Journal of Geophysical Research: Solid Earth*, *122*, 4492–4508. https://doi.org/10.1002/2016JB013769
Wang, Y., Lin, F.-C., & Ward, K. M. (2019). Ambient noise tomography across the Cascadia subduction zone using dense linear seismic arrays and double beamforming. *Geophysical Journal International*, *217*(3), 1668–1680. https://doi.org/10.1093/gji/ggz109

Wechsler, N., Rockwell, T. K., & Ben-Zion, Y. (2009). Application of high resolution DEM data to detect rock damage from geomorphic signals along the central San Jacinto Fault. *Geomorphology*, *113*, 82–96. https://doi.org/10.1016/j.geomorph.2009.06.007
Weng, H., Yang, H., Zhang, Z., & Chen, X. (2016). Earthquake rupture extents and coseismic slips promoted by damaged fault zones. *Journal of Geophysical Research: Solid Earth*, *121*, 4446–4457. https://doi.org/10.1002/2015JB012713
Xu, S., & Ben-Zion, Y. (2017). Theoretical constraints on dynamic pulverization of fault zone rocks. *Geophysical Journal International*, *209*, 282–296. https://doi.org/10.1093/gji/ggx033
Xu, S., Ben-Zion, Y., Ampuero, J. P., & Lyakhovsky, V. (2015). Dynamic Ruptures on a Frictional Interface with Off-Fault Brittle Damage: Feedback Mechanisms and Effects on Slip and Near-Fault Motion. *Pure and Applied Geophysics*, *172*, 1243. https://doi.org/10.1007/s00024-014-0923-7
Yang, H., Li, Z., Peng, Z., Ben-Zion, Y., & Vernon, F. (2014). Low-velocity zones along the San Jacinto Fault, Southern California, from body waves recorded in dense linear arrays. *Journal of Geophysical Research: Solid Earth*, *119*, 8976–8990. https://doi.org/10.1002/2014JB011548
Yang, H., & Zhu, L. (2010). Shallow low-velocity zone of the San Jacinto fault from local earthquake waveform modelling. *Geophysical Journal International*, *183*, 421–432. https://doi.org/10.1111/j.1365-246X.2010.04744.x
Yao, H., Beghein, C., & Hilst, R. D. (2006). Surface wave array tomography in SE Tibet from ambient seismic noise and two-station analysis—II. Crustal and upper-mantle structure. *Geophysical Journal International*, *166*, 205–219. https://doi.org/10.1111/j.1365-246X.2007.03696.x
Zigone, D., Ben-Zion, Y., Campillo, M., & Roux, P. (2015). Seismic tomography of the Southern California plate boundary region from noise-based Rayleigh and Love waves. *Pure and Applied Geophysics*, *172*(5), 1007–1032. https://doi.org/10.1007/s00024-014-0872-1
Zigone, D., Ben-Zion, Y., Lehujeur, M., Campillo, M., Hillers, G., & Vernon, F. L. (2019). Imaging subsurface structures in the San Jacinto fault zone with high-frequency noise recorded by dense linear arrays. *Geophysical Journal International*, *217*, 879–893. https://doi.org/10.1093/gji/ggz069